Accuracy of ghost-rotationally-invariant slave-boson theory for multiorbital Hubbard models and realistic materials

Tsung-Han Lee,[1,2,*] Corey Melnick,[3] Ran Adler,[1] Nicola Lanatà,[4,5] and Gabriel Kotliar[1,3]
[1]*Physics and Astronomy Department, Rutgers University, Piscataway, New Jersey 08854, USA*
[2]*Department of Physics, National Chung Cheng University, Chiayi 62102, Taiwan*
[3]*Condensed Matter Physics and Materials Science Department, Brookhaven National Laboratory, Upton, New York 11973, USA*
[4]*School of Physics and Astronomy, Rochester Institute of Technology, 84 Lomb Memorial Drive, Rochester, New York 14623, USA*
[5]*Center for Computational Quantum Physics, Flatiron Institute, New York, New York 10010, USA*

(Received 21 May 2023; revised 20 October 2023; accepted 6 December 2023; published 19 December 2023)

We assess the accuracy of ghost-rotationally-invariant slave-boson (g-RISB) theory in multiorbital systems by applying it to both the three-orbital degenerate Hubbard model and a realistic Sr_2RuO_4 model extracted from first-principle simulations and comparing the results to those obtained using dynamical mean-field theory (DMFT). Our findings indicate that g-RISB's accuracy can be systematically improved toward the exact DMFT limit in infinite-dimensional multiorbital models by increasing the number of ghost orbitals. This allows for a more precise description of aspects of Hund metal physics and Mott physics compared with the original RISB approach. We also demonstrate that g-RISB reliably captures the quasiparticle weights, Fermi surface, and low-energy spectral function for the realistic Sr_2RuO_4 model compared with DMFT. Moreover, we showcase the potential of using the density matrix renormalization group method as an impurity solver within the g-RISB framework to study systems with a larger number of ghost orbitals. These results show the potential of g-RISB as a reliable tool for simulating correlated materials. The connection between the g-RISB and DMFT self-energy is also discussed.

DOI: 10.1103/PhysRevB.108.245147

I. INTRODUCTION

The rotationally invariant slave-boson (RISB) mean-field theory [1,2], Gutzwiller approximation [3–9], and other slave-particle mean-field approaches are efficient methodologies for studying the strong correlation effects in multiorbital Hubbard models [10–17]. These approaches effectively capture the fundamental orbital-selective Mott physics and Hund's metallicity in multiorbital systems [12,18–23], exhibiting qualitative agreement with the more computationally demanding dynamical mean-field theory (DMFT) [24], and have been widely applied to investigate realistic materials, such as iron-based superconductors and heavy-fermion systems [25–33]. However, despite their success, the accuracy of slave-particle mean-field approaches and the Gutzwiller approximation is not always sufficient. For example, these approaches tend to overestimate the critical Coulomb interaction for Mott transitions due to the lack of descriptions of the charge fluctuation in the Mott insulating phase [34]. Hence, they require the use of larger Coulomb interactions to achieve experimentally observed Mott insulating behavior in transition-metal compounds [30]. Additionally, recent studies on Sr_2RuO_4 indicate that RISB significantly underestimates the effective mass of the electrons [35,36]. Therefore, it is desirable to have a systematic route to improve the accuracy of RISB.

Recently, the ghost-rotationally-invariant slave-boson (g-RISB) approach has been developed to improve the accuracy of the original RISB method [34,37,38]. The key concept of g-RISB is to enlarge the variational space of the original RISB by introducing auxiliary "ghost" degrees of freedom, where similar ideas have been developed simultaneously in different contexts of many-body approaches [39–42]. It has been shown that g-RISB with two additional ghost orbitals provides a reliable description of the Mott transition in single-orbital Hubbard and Anderson lattice models when compared with DMFT [34,37,43]. Moreover, the studies on the one-band Hubbard model have shown that the accuracy of g-RISB can be systematically improved toward the exact solution in infinite dimensions by increasing the number of ghost orbitals [44–46]. However, the accuracy of g-RISB as the number of ghost orbitals increases has not been explored in multiorbital systems. Recently, the g-RISB has been applied to multi-orbital systems focusing on the quasiparticle, spectral, and local atomic properties for multiorbital models on the Bethe lattice [47]. However, the energetics and the application of g-RISB to more realistic models of materials have not been explored. In particular, it would be desirable to explore if g-RISB can solve the above-mentioned limitations of RISB, i.e., the overestimation of the critical Coulomb interaction of the Mott transitions and the underestimation of the effective mass of Sr_2RuO_4 [30,35,36].

In this work, we assess the accuracy of g-RISB on the degenerate three-orbital Hubbard model and the realistic Sr_2RuO_4 model extracted from first-principle simulations

*tsunghan@ccu.edu.tw

by comparing the results with DMFT. For the degenerate three-orbital model, we demonstrate that g-RISB significantly enhances the accuracy of the original RISB approach, providing a more precise description of Hund's metallic behavior and Mott transition, where the critical point of the Mott transition is consistent with DMFT. Furthermore, we provide numerical evidence that the accuracy of g-RISB can be systematically improved toward the exact DMFT limit in infinite dimensions by increasing the number of ghost orbitals in the considered multiorbital models. For the realistic Sr_2RuO_4 model, our results illustrate that g-RISB captures reliable energy, quasiparticle weights, Fermi surface, and low-energy spectral function in good agreement with DMFT and experiments. Moreover, we present the capability of employing the density-matrix renormalization group (DMRG) method as the impurity solver within the g-RISB framework [48–50], enabling us to explore systems characterized by a larger number of ghost orbitals that are beyond the capacity of the exact diagonalization (ED) solver. In addition, we discuss the connection between the g-RISB and DMFT self-energy. Our benchmarks highlight the potential of g-RISB as a reliable tool for simulating strongly correlated materials.

II. MODEL

We consider the following three-orbital Hubbard model:

$$H = \sum_{\mathbf{k}} \sum_{ll'\sigma} \epsilon_{\mathbf{k}ll'} c^\dagger_{\mathbf{k}l\sigma} c_{\mathbf{k}l'\sigma} + \sum_{\mathbf{R}} H^{\mathrm{loc}}_{\mathbf{R}}[\{c^\dagger_{\mathbf{R}l\sigma}, c_{\mathbf{R}l\sigma}\}], \quad (1)$$

where $c^\dagger_{\mathbf{k}l\sigma}$ and $c_{\mathbf{k}l\sigma}$ are the electronic creation and the annihilation operators, respectively, with the orbital index l, the spin index σ, the momentum index $\mathbf{k}$, and the site index $\mathbf{R}$, and $\epsilon_{\mathbf{k}ll'}$ is the hopping dispersion. In this work, we focus on the $\epsilon_{\mathbf{k}ll'}$ corresponding to a degenerate semicircular density of states of the infinite-dimensional Bethe lattice and a realistic Sr_2RuO_4 dispersion extracted from the first-principle simulations. The local Hamiltonian $H^{\mathrm{loc}}_{\mathbf{R}}$ has the following form:

$$H^{\mathrm{loc}}_{\mathbf{R}}[\{c^\dagger_{\mathbf{R}l\sigma}, c_{\mathbf{R}l\sigma}\}] = \sum_{ll'\sigma} \epsilon^{\mathrm{loc}}_{\mathbf{R},ll'} c^\dagger_{\mathbf{R}l\sigma} c_{\mathbf{R}l'\sigma} + H^{\mathrm{int}}_{\mathbf{R}}[\{c^\dagger_{\mathbf{R}l\sigma}, c_{\mathbf{R}l\sigma}\}], \quad (2)$$

where $\epsilon^{\mathrm{loc}}_{\mathbf{R}ll'}$ is the local one-body interaction and

$$\begin{aligned} H^{\mathrm{int}}_{\mathbf{R}}[\{c^\dagger_{\mathbf{R}l\sigma}, c_{\mathbf{R}l\sigma}\}] &= U \sum_{l} n_{\mathbf{R}l\uparrow} n_{\mathbf{R}l\downarrow} + U' \sum_{l<l',\sigma} n_{\mathbf{R}l\sigma} n_{\mathbf{R}l'\bar{\sigma}} \\ &+ (U' - J) \sum_{l<l',\sigma} n_{\mathbf{R}l\sigma} n_{\mathbf{R}l'\sigma} \\ &- J \sum_{l<l'} (c^\dagger_{\mathbf{R}l\uparrow} c_{\mathbf{R}l\downarrow} c^\dagger_{\mathbf{R}l'\downarrow} c_{\mathbf{R}l'\uparrow} \\ &+ c^\dagger_{\mathbf{R}l\uparrow} c^\dagger_{\mathbf{R}l\downarrow} c_{\mathbf{R}l'\uparrow} c_{\mathbf{R}l'\downarrow} + \mathrm{H.c.}). \end{aligned} \quad (3)$$

is the Hubbard-Kanamori parametrization of the two-body Coulomb interaction [51]. In addition, we use the rotationally invariant condition $U' = U - 2J$. In the following, we also introduce the index $\alpha \equiv (l, \sigma)$ to combine the electronic spin and orbital degrees of freedom.

III. METHODS

A. Ghost-rotationally-invariant slave boson

Here, we describe the formalism of g-RISB for multiorbital models, which is the direct generalization of the previous works [34,37,38,44]. The g-RISB theory is encoded in the following Lagrange function:

$$\begin{aligned} &\mathcal{L}[\Phi, E^c; R, \lambda; D, \lambda^c; \Delta, \Psi_0, E] \\ &= \frac{1}{\mathcal{N}} \langle \Psi_0 | \hat{H}^{\mathrm{qp}}[R, \lambda] | \Psi_0 \rangle \\ &\quad + E(1 - \langle \Psi_0 | \Psi_0 \rangle) + [\langle \Phi | \hat{H}^{\mathrm{emb}}[D, \lambda^c] | \Phi \rangle \\ &\quad + E^c(1 - \langle \Phi | \Phi \rangle)] - \Bigg[\sum_{ab} [\lambda + \lambda^c]_{ab} [\Delta]_{ab} \\ &\quad + \sum_{ca\alpha} \left([D]_{a\alpha} [R]_{c\alpha} [\Delta(1 - \Delta)]^{\frac{1}{2}}_{ca} + \mathrm{c.c.} \right) \Bigg], \end{aligned} \quad (4)$$

where H^{qp} is the quasiparticle Hamiltonian, H^{emb} is the embedding Hamiltonian, and $|\Psi_0\rangle$ and $|\Phi_i\rangle$ are their corresponding wave functions, respectively. E and E^c are Lagrange multipliers enforcing the normalization of the wave functions. The λ and λ^c enforce the structure of the quasiparticle density matrix Δ, and D enforces the structure of the quasiparticle renormalization matrix R. $\mathcal{N}$ is the total number of sites in the lattice.

The quasiparticle Hamiltonian has the following form:

$$H^{\mathrm{qp}} = \sum_{\mathbf{k}} \sum_{ab} \sum_{\alpha\beta} [R_{a\alpha} \epsilon_{\mathbf{k},\alpha\beta} R^\dagger_{\beta b} + \lambda_{ab}] f^\dagger_{\mathbf{k}a} f_{\mathbf{k}b}, \quad (5)$$

where, for the three-orbital model, $\alpha, \beta \in \{1\uparrow, 1\downarrow, 2\uparrow, 2\downarrow, 3\uparrow, 3\downarrow\}$ labels the original physical degrees of freedom $c_{\mathbf{k}\alpha}$, and a, b labels the auxiliary quasiparticle degrees of freedom $f_{\mathbf{k}a}$. The number of quasiparticle orbitals can be systematically increased by adding the so-called ghost orbitals to improve the accuracy of g-RISB. In this work, we used up to fifteen auxiliary quasiparticle orbitals, i.e., $a, b \in \{1\uparrow, 1\downarrow, \ldots, 15\uparrow, 15\downarrow\}$ to study the convergence behavior of g-RISB in multiorbital Hubbard models. Note that, with the minimal three quasiparticle orbitals, $a, b \in \{1\uparrow, 1\downarrow, 2\uparrow, 2, \downarrow 3\uparrow, 3\downarrow\}$, g-RISB recovers the original RISB approach.

The embedding Hamiltonian is as follows:

$$\hat{H}^{\mathrm{emb}} = \hat{H}^{\mathrm{loc}}[\{\hat{c}^\dagger_\alpha, \hat{c}_\alpha\}] + \sum_{a\alpha} (D_{a\alpha} \hat{c}^\dagger_\alpha \hat{f}_a + \mathrm{H.c.}) + \sum_{ab} \lambda^c_{ab} \hat{f}_b \hat{f}^\dagger_a, \quad (6)$$

where $\hat{c}^\dagger_\alpha$ and $\hat{c}_\alpha$ are the impurity creation and annihilation operators, respectively, and $\hat{f}^\dagger_a$ and $\hat{f}_a$ are the bath creation and annihilation operators, respectively. We use N_b to label the number of the bath orbitals. Note that the number of the bath orbitals is the same as the number of the quasiparticle orbitals in H^{qp}. The schematic representation of the two models is shown in Fig. 1.

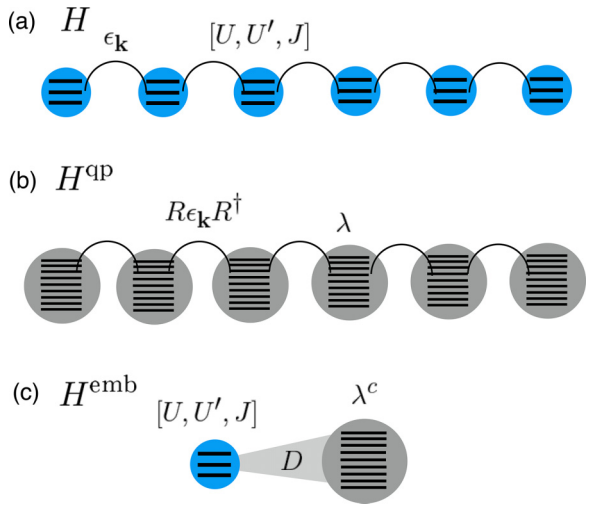

FIG. 1. Schematic representation of the (a) original three-orbital Hubbard Hamiltonian H, (b) the noninteracting quasiparticle Hamiltonian H^{qp} including enlarged auxiliary ghost degrees of freedom with in total nine orbitals, and (c) the embedding Hamiltonian H^{emb} including an impurity with three orbitals and a bath with nine orbitals. The number of the orbitals in the bath of H^{emb} and in H^{qp} can be increased simultaneously by introducing more ghost orbitals to improve the g-RISB accuracy. Here we illustrate the Hamiltonians at bath size $N_b = 9$.

The stationary condition of the g-RISB Lagrange function leads to the following saddle-point equations:

$$\frac{1}{\mathcal{N}}\left[\sum_{\mathbf{k}} n_{\mathrm{F}}(R\epsilon_{\mathbf{k}}R^{\dagger} + \lambda)\right]_{ba} = \Delta_{ab}, \tag{7}$$

$$\frac{1}{\mathcal{N}}\left[\sum_{\mathbf{k}} \epsilon_{\mathbf{k}}R^{\dagger} n_{\mathrm{F}}(R\epsilon_{\mathbf{k}}R^{\dagger} + \lambda)\right]_{ba} = \sum_{ac\alpha} D_{c\alpha}[\Delta(I-\Delta)]^{\frac{1}{2}}_{ac}, \tag{8}$$

$$\sum_{cd\alpha} \frac{\partial}{\partial \Delta_{ab}}\left([\Delta(I-\Delta)]^{\frac{1}{2}}_{cd} D_{d\alpha}R_{c\alpha} + \mathrm{c.c.}\right) + [\lambda + \lambda^{c}]_{ab} = 0, \tag{9}$$

$$\hat{H}^{\mathrm{emb}}|\Phi\rangle = E^{c}|\Phi\rangle, \tag{10}$$

$$\langle\Phi|\hat{c}^{\dagger}_{\alpha}\hat{f}_{a}|\Phi\rangle - \sum_{c}[\Delta(I-\Delta)]^{\frac{1}{2}}_{ac}R_{c\alpha} = 0, \tag{11}$$

$$\langle\Phi|\hat{f}_{b}\hat{f}^{\dagger}_{a}|\Phi\rangle - \Delta_{ab} = 0, \tag{12}$$

where n_F is the Fermi function, I is the identity matrix, and the variables R, λ, Δ, D, λ^c, and $|\Phi\rangle$ are determined self-consistently. Equations (7)–(12) have been rigorously derived in Refs. [34,37,38]. Here, we provide a simplified physical rationale to elucidate their meaning following Refs. [28,52,53]. As in any quantum embedding method, there are three basic ingredients: a high-level description of a local system (the embedding Hamiltonian $\hat{H}^{\mathrm{emb}}$ parametrized by D and λ^c), a low-level description of the lattice system (the quasiparticle Hamiltonian H^{qp} parametrized by R and λ), and compatibility conditions that establish a self-consistent linkage between the parameters of these two systems. For a given set of parameters, equations (7) and (10) provide us with the density matrix and the ground-state wave function of the two reference systems, respectively. The remaining saddle-point equations then utilize these quantities to determine a new set of parameters of both systems for self-consistency calculations (see Appendix A for our algorithm).

For the impurity solver of H_{emb}, we utilize the Lanczos ED algorithm to compute the ground-state wave function $|\Phi\rangle$ for bath size $N_b \leqslant 9$. To explore the accuracy at a larger bath size $N_b = 15$, it is necessary to utilize the DMRG approach to solve the ground-state wave function [48–50] because the Hilbert space is too large for performing the Lanczos ED. In this work, we utilize the DMRG implemented in Block2 and PySCF as our impurity solver [54–57].

With the converged R and λ, one can compute the Green's function from

$$G_{\alpha\beta}(\mathbf{k}, \omega) = \sum_{ab} R^{\dagger}_{\alpha a}[(\omega + i0^{+})I - R\epsilon_{\mathbf{k}}R^{\dagger} - \lambda]^{-1}_{ab}R_{b\beta}, \tag{13}$$

and the self-energy can be determined from the Dyson equation

$$\Sigma_{\alpha\beta}(\omega) = \left[G_0^{-1}(\mathbf{k}, \omega) - G^{-1}(\mathbf{k}, \omega)\right]_{\alpha\beta}, \tag{14}$$

where $G_0(\mathbf{k}, \omega)$ is the bare Green's function. The quasiparticle renormalization weight is determined from

$$Z_{\alpha\beta} = \left[1 - \frac{\partial \mathrm{Re}\Sigma(\omega)}{\partial\omega}\bigg|_{\omega\to 0}\right]^{-1}_{\alpha\beta}. \tag{15}$$

An expression for the g-RISB self-energy has been derived in the previous work [34,37,53], resulting into a pole-expansion representation. In this work, we exploit the gauge freedom [1,34,37] to provide a more compact expression and provide further insight into the connection between RISB and the DMFT self-energy. Specifically, we choose a gauge transforming R and λ into the following block matrix form:

$$u^{\dagger}R = \tilde{R} = \begin{pmatrix}\tilde{R}_0 \\ 0\end{pmatrix}, \quad u^{\dagger}\lambda u = \tilde{\lambda} = \begin{pmatrix}\tilde{\lambda}_0 & \tilde{\lambda}_1 \\ \tilde{\lambda}_1^{\dagger} & \tilde{\lambda}_2\end{pmatrix}, \tag{16}$$

where u is the gauge transformation matrix [1,29], $\tilde{R}^0$ and $\tilde{\lambda}^0$ are square matrices of size $N \times N$, where N is the total number of physical spin-orbitals. The matrix $\tilde{\lambda}_1$ is a $N \times M$ matrix where $M = 2N_b - N$, and $\tilde{\lambda}_2$ is a $M \times M$ diagonal matrix. This specific gauge always exist and the transformation matrix u can be calculated using the singular value decomposition method [53]. From Eq. (13), one can show that the self-energy has the following form:

$$\Sigma_{\alpha\beta}(\omega) = \omega[I - [\tilde{R}_0^{\dagger}\tilde{R}_0]^{-1}]_{\alpha\beta} + \sum_{ab}[\tilde{R}_0]^{-1}_{\alpha a}[\tilde{\lambda}_0]_{ab}[\tilde{R}_0^{\dagger}]^{-1}_{b\beta} - [\epsilon^{\mathrm{loc}}]_{\alpha\beta} + \sum_{abc}[\tilde{R}_0]^{-1}_{\alpha a}\frac{[\tilde{\lambda}_1]_{ac}[\tilde{\lambda}_1^{\dagger}]_{bc}}{[(\omega + i0^{+})I - \tilde{\lambda}_2]_{cc}}[R_0^{\dagger}]^{-1}_{b\beta}. \tag{17}$$

In this work, we provide numerical evidence that $\tilde{R}^{\dagger}\tilde{R}$, which equals the total spectral weight:

$$[\tilde{R}^{\dagger}\tilde{R}]_{\alpha\beta} = -\frac{1}{\mathcal{N}\pi}\sum_{\mathbf{k}}\int_{-\infty}^{\infty} d\omega \mathrm{Im}[G(\mathbf{k}, \omega)]_{\alpha\beta}, \tag{18}$$

approaches the identity as one increases the number of the ghost orbitals (see Appendix B). In this limit, the expression above simplifies further, as the first term in Eq. 17 vanishes. We have also checked numerically that $\Sigma(\infty)$ approaches the Hartree-Fock self-energy with increasing ghost orbitals (see Appendix B). The equation above, obtained from g-RISB principles, closely resembles the pole expansion proposed in previous DMFT literature [58]. Also, Eq. (17) implies the number of poles in the self-energy grows linearly with the number of ghost orbitals.

B. Dynamical mean-field theory

We also perform the DMFT calculations to compare with g-RISB. To benchmark the accuracy with respect to the number of the bath orbitals, we utilize DMFT with the Lanczos ED solver (DMFT-ED) with discretized bath orbitals, which has been applied to multiorbital models [59–69]. The hybridization function scheme is used for the bath fitting procedure with weight function $1/\omega_n$ [70], allowing stabler convergences for all the considered parameters. A fictitious temperature $\beta = 200$ is introduced for the bath fitting. The Lanczos algorithm is utilized to compute the ground-state wave functions and Green's functions. In addition, we performed the DMFT calculations with the continuous-time quantum Monte Carlo (CTQMC) solver implemented in the TRIQS library, providing us the exact solution for the benchmark [71–74].

IV. RESULTS

A. Degenerate three-orbital Hubbard model

We first apply the g-RISB approach to the degenerate three-orbital Hubbard model focusing on Hund's metal regime with Hund's coupling fixed at $J = 0.25U$, where the positive Hund's rule coupling generates high-spin incoherent Hund's metallic states away from half filling [19–21]. We consider the semicircular density of states $N(\omega) = \frac{1}{\pi t}\{1 - [\omega/(2t)]^2\}^{1/2}$ with the energy unit set to half bandwidth $D = 2t = 1$, corresponding to the $\epsilon_{\mathbf{k}l\sigma}$ on the Bethe lattice in the limit of infinite coordination [24].

The quasiparticle weights Z for g-RISB and RISB are shown in Fig. 2. From the density plot of the quasiparticle weights in Figs. 2(a) and 2(b), we found that the g-RISB quasiparticle weight is much smaller than the original RISB approach in the Hund's metal regime. In particular, for the electron filling $n = 2$ relevant for Sr_2RuO_4 and iron-based superconductors, the quasiparticle weights are around $Z \gtrsim 0.5$ even with large Coulomb interactions. On the other hand, the quasiparticle weights in g-RISB are about $Z \approx 0.2$ at large Coulomb interactions, which are strongly correlated. In Figs. 2(c) and 2(d), we show the corresponding quasiparticle weights Z as a function of Coulomb interaction for various fillings n. At half filling, $n = 3$, the Mott transition for g-RISB and RISB is at $U_c = 1.25$ and $U_c = 1.6$, respectively. We found that RISB is quantitatively reliable only around half filling $n = 3$ and becomes less accurate away from half filling. The overestimation of the quasiparticle weights in RISB, i.e., the underestimation of the effective mass, is also observed in the previous studies of Sr_2RuO_4, whose values deviate

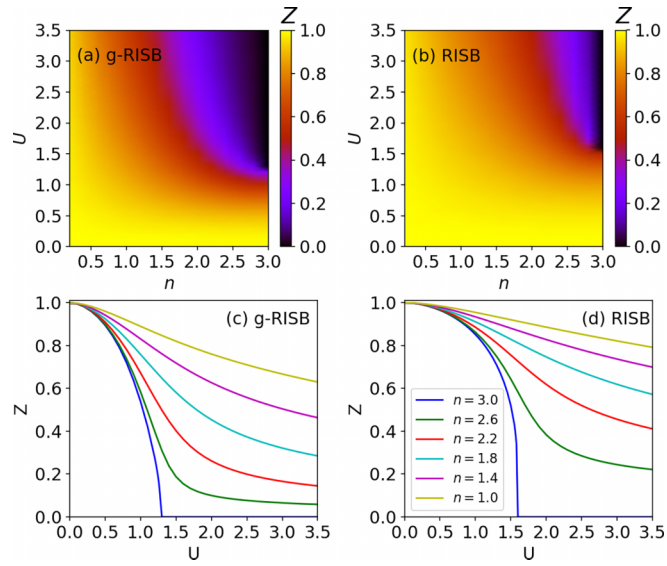

FIG. 2. Panels (a) and (c) show the quasiparticle weights Z for the degenerate three-orbital Hubbard model on Bethe lattice from g-RISB with $N_b = 9$ bath orbitals, and panels (b) and (d) show the quasiparticle weights of RISB (g-RISB with $N_b = 3$) as a function of Coulomb interaction U with $J = 0.25U$ for different electron filling n. The energy unit is the half bandwidth.

significantly from the DMFT values and experiments even using larger Coulomb parameters [35,36].

We now examine the accuracy of g-RISB closely as a function of Coulomb interactions at half filling $n = 3$. The corresponding quasiparticle weights Z, kinetic energy E^{kin}, potential energy E^{pot}, and total energy E^{tot} are shown in Fig. 3 for g-RISB, DMFT-ED, and DMFT-CTQMC. We observed that the g-RISB energy and quasiparticle weights converge systematically to the DMFT-CTQMC values with increasing bath orbitals N_b. With bath size $N_b = 9$, g-RISB already gives reliable energy and quasiparticle weights close to the exact DMFT-CTQMC values. On the other hand, the DMFT-ED results still have a slight discrepancy from the exact DMFT-CTQMC values, especially around the metal-insulator transition U_c. Moreover, g-RISB captures more precisely the discontinuity in the quasiparticle weights and the energy at U_c [75], and the accuracy in the quasiparticle weights can be further improved by increasing the bath size to $N_b = 15$. To have a closer look at the accuracy of g-RISB, we also show the g-RISB total energy E_{tot} for the selected Coulomb interactions U for different bath sizes N_b in Table I.

In Fig. 4, we benchmarked the accuracy of g-RISB as a function of Coulomb interactions U at electron filling $n = 2$, corresponding to the parameter regime of Hund's metal materials, e.g., Sr_2RuO_4 and iron-based superconductors. We observed that the accuracy of g-RISB is systematically improvable with the increasing number of bath orbitals N_b. With $N_b = 9$, g-RISB produces accurate energy close to the exact DMFT-CTQMC values, while DMFT-ED shows slight differences from the exact DMFT-CTQMC values. On the other hand, DMFT-ED gives accurate quasiparticle weights Z at $N_b = 9$, while g-RISB requires $N_b = 15$ bath orbitals to have similar accuracy. To have a closer look at the g-RISB

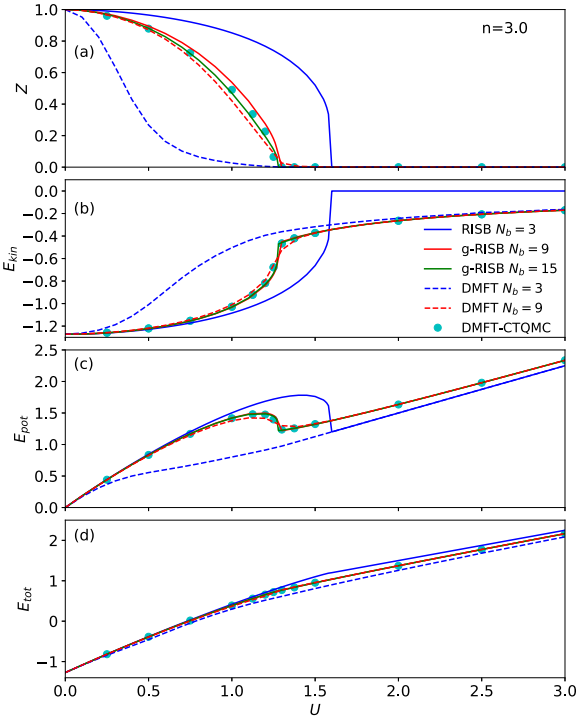

FIG. 3. (a) Quasiparticle weights Z, (b) kinetic energy E_{kin}, (c) potential energy E_{pot}, and (d) total energy E_{tot} for the degenerate three-orbital model on Bethe lattice for g-RISB with bath size $N_b = 3$, 9, 15 and DMFT-ED with $N_b = 3$, 9 as a function of Coulomb interaction U with Hund's coupling $J = 0.25U$ at filling $n = 3$. The DMFT-CTQMC results at inverse temperature $\beta = 200$ are shown for comparison. The energy unit is the half bandwidth.

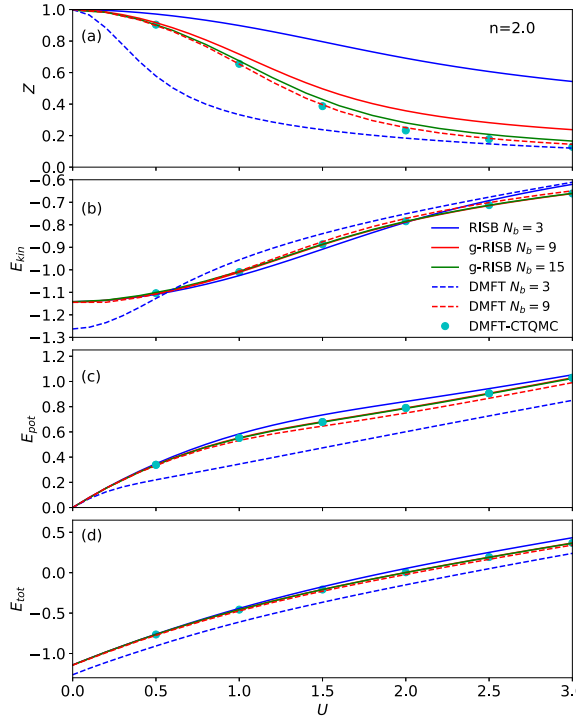

FIG. 4. (a) The quasiparticle weights Z, (b) kinetic energy E_{kin}, (c) potential energy E_{pot}, and (d) total energy E_{tot} for the degenerate three-orbital model on Bethe lattice for g-RISB with bath size $N_b = 3$, 9, 15 and DMFT-ED with $N_b = 3$, 9 as a function of Coulomb interaction U with Hund's coupling $J = 0.25U$ at filling $n = 2$. The DMFT-CTQMC results at inverse temperature $\beta = 200$ are shown for comparison. The energy unit is the half bandwidth.

energy, we show the total energy for the selected parameters in Table I.

Figure 5 shows the spectral functions $A(\omega) = -\text{Im}G(\omega)/\pi$ for several sets of parameters in the degenerate three-orbital model. For RISB $N_b = 3$, the metal-insulator transition is of the Brinkman-Rice scenario, where only the band renormalization around the Fermi level is captured, and the incoherent Hubbard bands are absent. Therefore, for $n = 3$ and $U = 3$, the spectral function is zero, which is a crude approximation to the Mott insulator. On the other hand, for $N_b = 9$, g-RISB can capture both the coherent quasiparticle peak and the Hubbard bands, and the quality of the spectral functions can be systematically improved by adding more bath orbitals to $N_b = 15$. Furthermore, the overall position of the peaks in the g-RISB spectral functions is in good agreement with the DMFT-ED and DMFT-CTQMC spectral functions. These results suggest that while g-RISB can capture reliable energy, the spectral functions require more bath orbitals to reach a similar accuracy to DMFT-ED. In addition, since g-RISB with a small number of ghost orbitals cannot reliably capture the finite scattering rate in the imaginary part of the self-energy (see Appendix C), its high-energy spectral function becomes more coherent than DMFT-CTQMC. This is also a feature in DMFT-ED with a small number of bath orbitals, where the exponentially large number of poles tends to cluster together forming sharp features in the spectrum, see Fig. 5 and Refs. [24,59,60].

TABLE I. The g-RISB total energy E_{tot} for the degenerate three-orbital model on Bethe lattice for the selected fillings n and U with different numbers of bath orbitals N_b and $J = 0.25U$. The DMFT energy at $\beta = 200$ with CTQMC solver is shown for comparison. The energy unit is the half bandwidth.

n	U	$N_b = 3$	$N_b = 9$	$N_b = 15$	DMFT-CTQMC
3.0	1.0	0.412	0.389	0.388	0.389
3.0	2.5	1.875	1.774	1.773	1.772
2.0	1.5	−0.174	−0.208	−0.209	−0.208
2.0	2.5	0.2506	0.192	0.189	0.193

B. Realistic Sr_2RuO_4 model

In this section, we present the results for Sr_2RuO_4, which is a well-characterized bad metal driven by Hund's physics [76,77]. The experimental quasiparticle weights are $Z^{\text{expt}}_{xz/yz} \approx 0.33$ and $Z^{\text{expt}}_{xy} \approx 0.18$ for the three orbitals in the t_{2g} subshell [76,78].

First, we construct the realistic tight-binding model from density functional theory (DFT) [79,80] and maximally localized Wannier function [81]. We utilized WIEN2K with 10 000 k points and the local density approximation (LDA) functional for our DFT calculations [82]. The lattice parameters utilized in our DFT calculations are derived from the

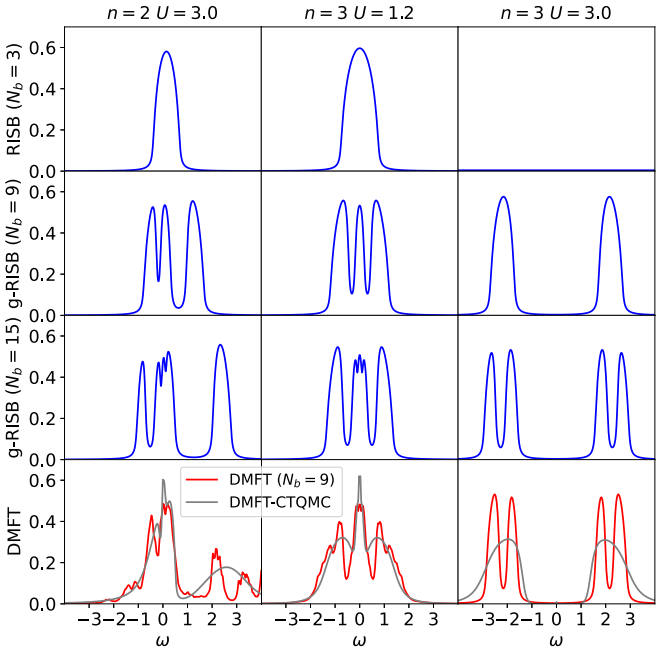

FIG. 5. The g-RISB spectral functions $A(\omega)$ with bath size $N_b = 3$, 9, 15 compared with the DMFT spectral function using ED solver with $N_b = 9$ and CTQMC solver for electron filling $n = 2$ and Coulomb $U = 3$ (the first column), $n = 3$ and $U = 1.2$ (the second column), and $n = 3$ and $U = 3$ (the third column). The Hund's coupling is $J = 0.25U$. The inverse temperature in the DMFT-CTQMC calculations is $\beta = 200$, and the energy unit is the half bandwidth. A broadening factor $\eta = 0.05$ is used in the ED and g-RISB.

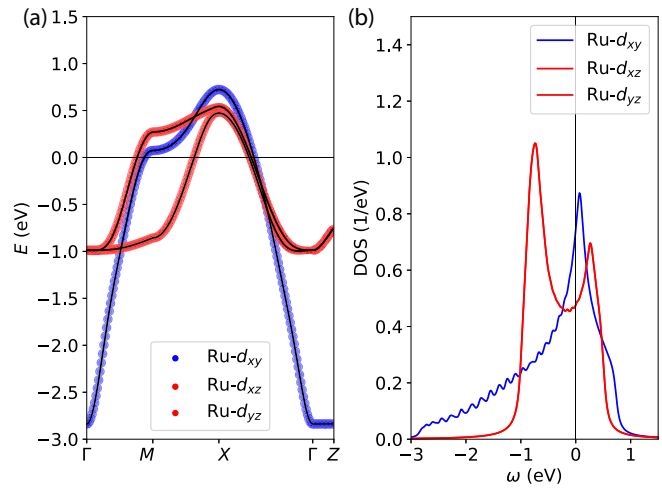

FIG. 6. (a) The Wannier tight-binding band structure for Sr_2RuO_4 extracted from density functional theory along the high-symmetry path in the Brillouin zone and (b) the orbital-resolved density of states constructed from the density functional theory considering the Ru-d_{xy}, d_{xz}, and d_{yz} orbitals. A broadening factor $\eta = 0.05$ is used in the density of states.

experimental structure at 100 K in Ref. [83]. The tetrahedron method is utilized for the Brillouin-zone integration [84]. The WIEN2WANNIER and WANNIER90 packages are then applied to construct the low-energy tight-binding model [85,86]. The low-energy tight-binding model is constructed from the Ru-d_{xy}, d_{xz}, and d_{yz} orbitals with the energy window $[-3$ eV, 1 eV], and $10 \times 10 \times 10$ k points. The spin-orbit coupling is ignored for simplicity. The Wannier tight-binding dispersion constructed from DFT is shown in Fig. 6. The d_{xz} and d_{yz} orbitals show a degenerate quasi-one dimensional density of states, and the d_{xy} orbital has a two-dimensional dispersion with a van Hove singularity at the Fermi level.

Next, we apply RISB to include the electronic correlation effect. Figures 7(a) and 7(b) show the momentum-resolved spectral function $A(\mathbf{k}, \omega)$ along the high-symmetry path in the Brillouin zone and the orbital-resolved density of states for RISB, respectively, at $U = 2.3$ eV and $J = 0.4$ eV. We found that the overall band structure is similar to DFT, with a slight renormalization of the bandwidth. The quasiparticle weights for each orbital are $Z_{xz/yz}^{\mathrm{RISB}} = 0.67$ and $Z_{xy}^{\mathrm{RISB}} = 0.66$, which are inconsistent with the experiments. This behavior has been reported in Refs. [35,36].

We now discuss the g-RISB spectral function and density of states shown in Figs. 7(c) and 7(d), respectively. We use $N_b = 9$ bath orbitals in our g-RISB calculations, so the total number of orbitals in the embedding Hamiltonian is $N_{\mathrm{tot}} = 12$, which can be efficiently solved by ED. The g-RISB band structure contains three groups of bands. The bands around

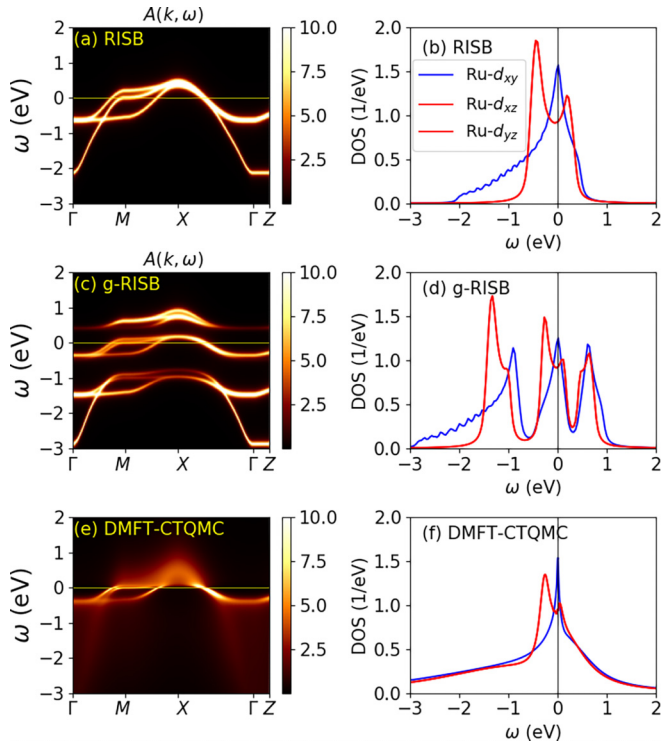

FIG. 7. (a) The momentum-resolved spectral function $A(\mathbf{k}, \omega)$ along the high-symmetry path in the Brillouin zone and (b) the orbital-resolved density of states for Sr_2RuO_4 from RISB with $U = 2.3$ eV and $J = 0.4$ eV. (c) The momentum-resolved spectral function $A(\mathbf{k}, \omega)$ and (d) the orbital-resolved density of states from g-RISB with bath size $N_b = 9$ at the same Coulomb parameters. (e) The momentum-resolved spectral function $A(\mathbf{k}, \omega)$ and (f) the orbital-resolved density of states from DMFT with CTQMC solver with $U = 2.3$ eV, $J = 0.4$ eV, and $\beta = 200$ eV^{-1}. A broadening factor $\eta = 0.05$ is used in the density of states.

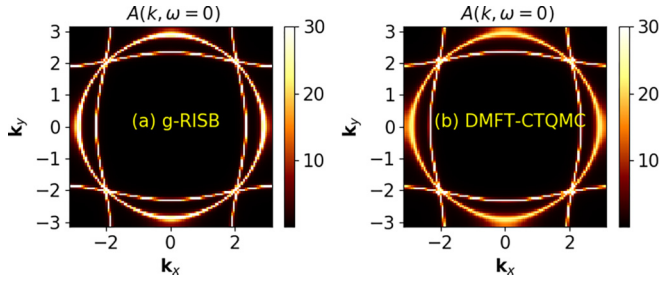

FIG. 8. The momentum resolved spectral function for Sr_2RuO_4 at $\omega = 0$, i.e., the Fermi surface, from (a) g-RISB with bath size $N_b = 9$ for $U = 2.3$ eV and $J = 0.4$ eV and (b) DMFT with CTQMC solver for $U = 2.3$ eV and $J = 0.4$ eV and $\beta = 200$ eV^{-1}. A broadening factor $\eta = 0.05$ is used in the g-RISB density of states.

the Fermi level $\omega = 0$ are the strongly renormalized quasiparticle bands. The quasiparticle weights are $Z_{xz/yz}^{\text{g-RISB}} = 0.4$ and $Z_{xy}^{\text{g-RISB}} = 0.35$ for each orbital, in reasonable agreement with experiments and the DMFT studies [76,87–91]. The bands located at the energy windows $[-3\text{ eV}, -0.5\text{ eV}]$ and $[0.2\text{ eV}, 0.6\text{ eV}]$ correspond to the lower and upper Hubbard bands, respectively. The DMFT results with CTQMC solver are shown in Figs. 7(e) and 7(f), reproducing the previous studies with $Z_{xz/yz}^{\text{DMFT}} = 0.3$ and $Z_{xz/yz}^{\text{DMFT}} = 0.2$ [90,91]. Our results show that g-RISB is able to accurately capture the low-energy quasiparticle bands around the Fermi level compared with DMFT. On the other hand, although the Hubbard bands in g-RISB locate at the correct energy scales, they do not have the incoherent feature in DMFT, with smeared dispersive bands. We also show the Fermi surface in Fig. 8 for g-RISB with $N_b = 9$ and DMFT with CTQMC solver. The g-RISB Fermi surface is in excellent agreement with DMFT.

The quasiparticle weights for g-RISB, RISB, and DMFT as a function of Coulomb interaction U with $J = 0.2U$ are shown in Figs. 9(a) and 9(b). The RISB quasiparticle weights are overestimated even at large Coulomb interactions ($Z \approx 0.6$ around $U = 3.0$ eV) compared with the values observed in experiments ($Z_{xz/yz}^{\text{expt}} \approx 0.33$ and $Z_{xy}^{\text{expt}} \approx 0.18$). In addition, the quasiparticle weight in the d_{xy} orbital is always larger than the $d_{xz/yz}$ orbitals for all the Coulomb interactions U, which is inconsistent with the experiments and the DMFT values. On the other hand, g-RISB significantly improves the RISB quasiparticle weights toward the DMFT values for the considered interactions U, and the accuracy can be systematically improved with increasing N_b. The kinetic energy E_{kin} and potential energy E_{pot} are shown in Figs. 9(c) and 9(d), respectively. We observed that RISB already provides accurate energy for this model, and the energy is almost indistinguishable from DMFT for g-RISB with $N_b = 9$. To have a closer comparison with DMFT, we also provide the total energy values in Table II for the selected parameters.

C. Discussions

The numerical results presented here and in the previous studies on the one-orbital Hubbard model [37,44–46] strongly suggest that the total energy within g-RISB converges to the DMFT total energy from above as the number of ghost orbitals

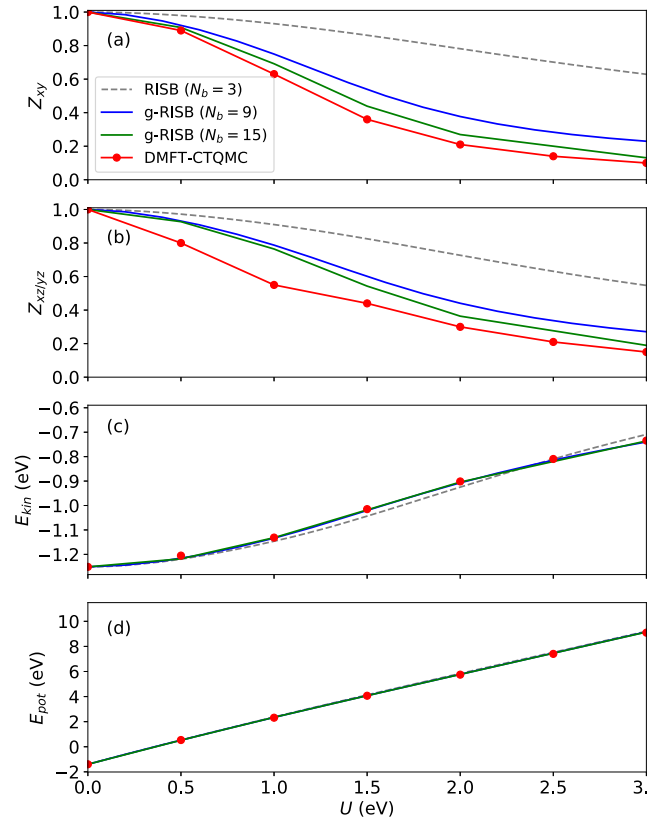

FIG. 9. The g-RISB and RISB quasiparticle weights for (a) the xy orbital Z_{xy}, (b) the xz/yz orbital $Z_{xz/yz}$, (c) the kinetic energy E_{kin}, and (d) the potential energy E_{pot} for Sr_2RuO_4 as a function of Coulomb interaction U with $J = 0.2U$ and bath size $N_b = 3$, 9, 15. The DMFT results with CTQMC solver at $\beta = 200$ eV^{-1} are shown for comparison.

is increased. The g-RISB spectral functions also approach the DMFT spectral functions as the number of bath orbitals in the embedding problem increases. For a given number of bath sites, we observe that g-RISB generally provides more accurate total energy, while DMFT-ED performs better for spectral properties. An analogous situation occurs within electronic structure methods: density functional theory, which targets the exact density of the materials, provides a good approximation to the densities but is less precise for the spectral properties. On the other hand, the more expensive spectral density functional theory, which targets the spectra [92,93], yields better results for spectral observables. Likewise, we can view g-RISB as an approximation to an exact density-matrix

TABLE II. The g-RISB total energy E_{tot} for the Sr_2RuO_4 model with different numbers of bath orbitals N_b at $U = 1.5$ eV and 2.5 eV. The Hund's coupling is $J = 0.2U$, and the electron filling is $n = 4$. The DMFT energy at $\beta = 200$ eV^{-1} with the CTQMC solver is shown for comparison. The energy unit is in electron volts.

U	$N_b = 3$	$N_b = 9$	$N_b = 15$	DMFT-CTQMC
1.5	3.0895	3.056	3.055	3.053
2.5	6.718	6.649	6.646	6.648

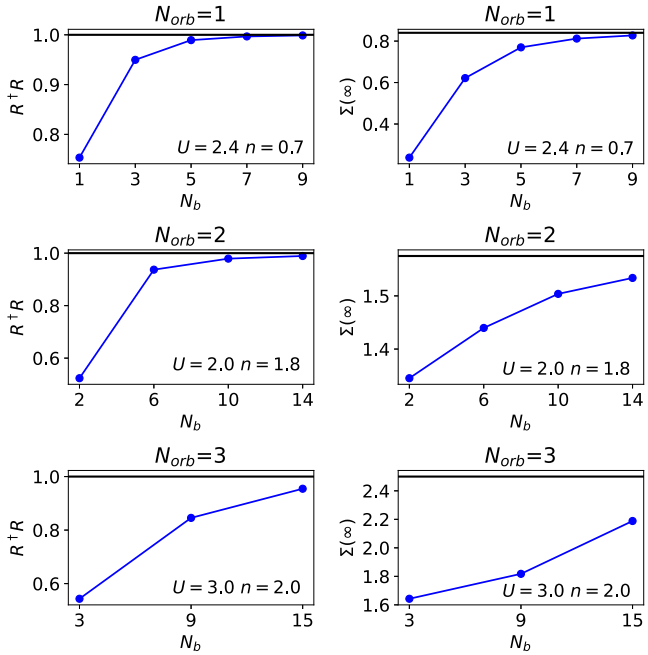

FIG. 10. The diagonal element of $R^\dagger R$ and the self-energy at infinity frequency $\Sigma(\infty)$ as a function of the number of the bath orbitals N_b for the degenerate one-orbital $N_{\rm orb} = 1$, two-orbital $N_{\rm orb} = 2$, and three-orbital $N_{\rm orb} = 3$ Hubbard model. The Coulomb parameters U and electron fillings n are given in the figures. The $R^\dagger R$ and $\Sigma(\infty)$ approach one and the Hartree-Fock self-energy (the horizontal lines), respectively.

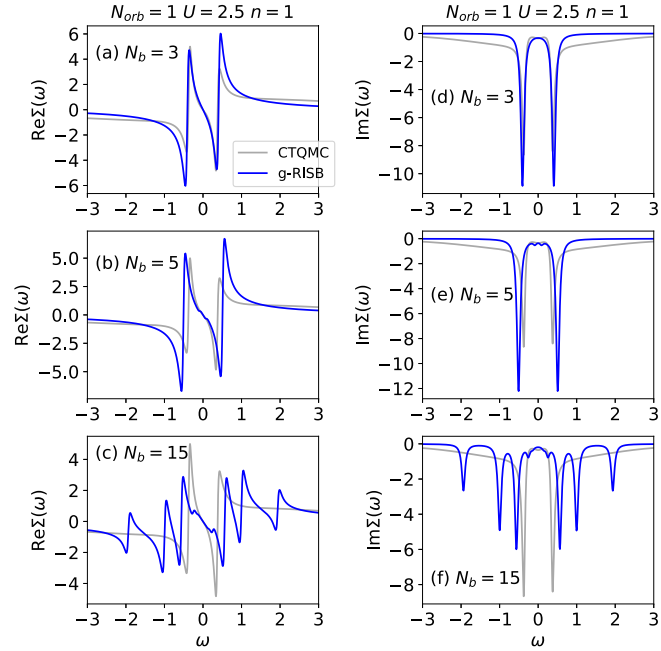

FIG. 11. (a)–(c) The real part of the g-RISB self-energy, $\mathrm{Re}\,\Sigma(\omega)$, for the one-orbital Hubbard model with increasing number of bath orbitals $N_b = 3$–15. (d)–(f) The imaginary part of the g-RISB self-energy, $\mathrm{Im}\,\Sigma(\omega)$, for the one-orbital Hubbard model with an increasing number of bath orbitals $N_b = 3$–15. A broadening factor $\eta = 0.05$ is used, and the energy unit is the half bandwidth. The DMFT-CTQMC self-energy (gray lines) with temperature $\beta = 200$ is shown for comparison.

functional theory, which targets the exact one body density matrix [94], in the same spirit that DMFT can be viewed as an approximation to an exact spectral density functional [93,95]. From these perspectives, we can understand why RISB gives good approximations to the total energy, while the spectra are clearly insufficient as the total spectral weight is too small, and why adding more ghost sites in g-RISB rapidly improves the total energy. The expression of the g-RISB self-energy, which is similar to the DMFT pole expansion (Eq. (17), calls for further exploration of the connections between these two methods.

V. CONCLUSIONS

We applied the g-RISB approach to the degenerate three-orbital Hubbard and a realistic Sr_2RuO_4 model and benchmarked its accuracy with DMFT. We provide numerical evidence that the accuracy of g-RISB is systematically improvable toward the exact DMFT limit in infinite-dimensional multiorbital models with an increasing number of ghost orbitals. This allows a more precise description of Hund's metal behavior and Mott transition compared with the original RISB approach. Moreover, we apply g-RISB to a realistic Sr_2RuO_4 model extracted from density functional theory and show that it produces reliable quasiparticle weights, Fermi surface, and low-energy spectral function, compared with DMFT and experiments. Furthermore, we showcase the capability of employing the DMRG method as the impurity solver within the g-RISB framework, allowing us to explore systems with a greater number of ghost orbitals beyond the reach of the ED solver. The connection between the g-RISB and the DMFT self-energy was also discussed.

Our results demonstrate that g-RISB is a promising approach to strongly correlated materials that can be combined with first-principle simulations. Future research will focus on the effect of spin-orbit coupling, the development of charge self-consistent DFT + g-RISB [28,92,96], the accuracy of the g-RISB response functions [97], and the potential of utilizing other tensor network approaches as a g-RISB impurity solver [91,98].

ACKNOWLEDGMENTS

We thank Antoine Georges for the useful discussions. T.-H.L, R.A., and G.K. were supported by the U.S. Department of Energy, Office of Science, Office of Advanced Scientific Computing Research, and Office of Basic Energy Sciences, Scientific Discovery through Advanced Computing (SciDAC) program under Award No. DE-SC0022198. This work was supported by the U.S. Department of Energy, Office of Basic Energy Sciences as part of the Computation Material Science Program. N.L. gratefully acknowledges funding from the Simons Foundation (Grant No. 1030691, N.L.) and the Novo Nordisk Foundation through the Exploratory Interdisciplinary Synergy Programme Project No. NNF19OC0057790. T.-H.L. gratefully acknowledges funding from the Ministry of Science

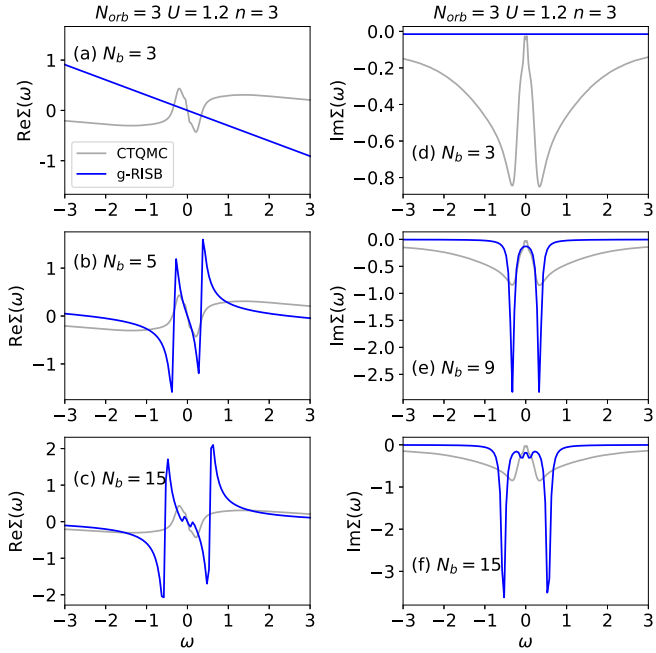

FIG. 12. (a)–(c) The real part of the g-RISB self-energy, $\mathrm{Re}\Sigma(\omega)$, for the degenerate three-orbital Hubbard model with increasing number of bath orbitals $N_b = 3$–15. (d)–(f) The imaginary part of the g-RISB self-energy, $\mathrm{Im}\Sigma(\omega)$, for the degenerate three-orbital Hubbard model with an increasing number of bath orbitals $N_b = 3$–15. A broadening factor $\eta = 0.05$ is used, and the energy unit is the half bandwidth. The DMFT-CTQMC self-energy (gray lines) with temperature $\beta = 200$ is shown for comparison.

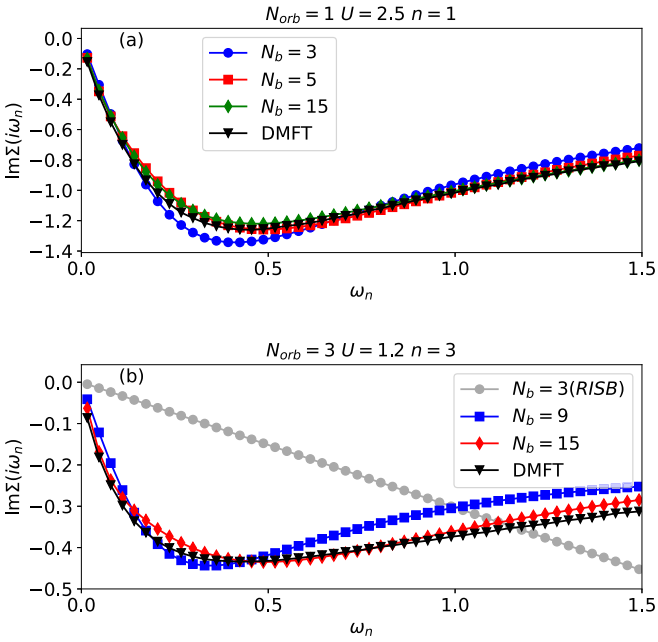

FIG. 13. (a) The imaginary part of the g-RISB self-energy, $\mathrm{Im}\Sigma(i\omega_n)$, on the Matsubara axis for the one-orbital Hubbard model with increasing number of bath orbitals $N_b = 3$–15. (b) The imaginary part of the g-RISB self-energy, $\mathrm{Im}\Sigma(\omega)$, for the degenerate three-orbital Hubbard model with an increasing number of bath orbitals $N_b = 3$–15. The energy unit is the half bandwidth. The DMFT-CTQMC self-energy (gray symbols) with temperature $\beta = 200$ is shown for comparison.

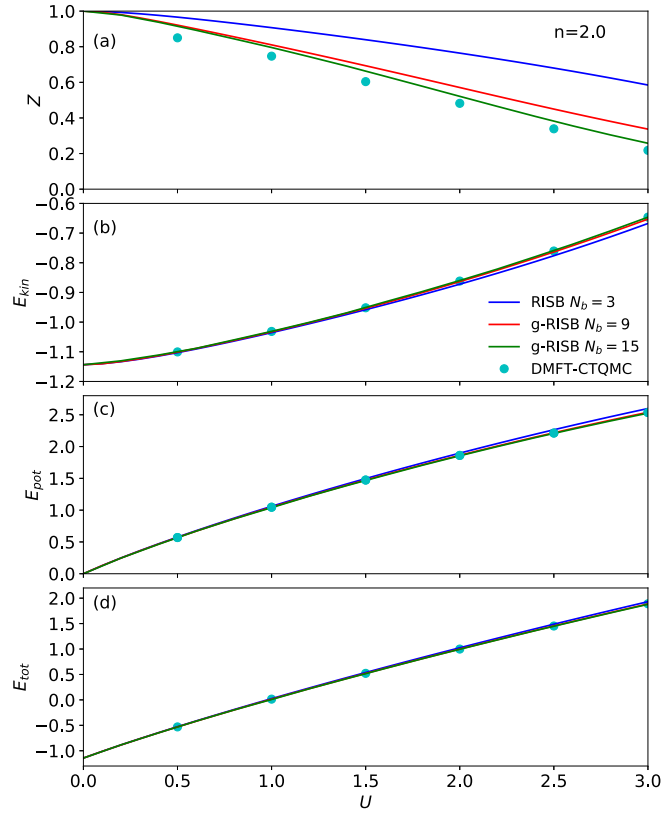

FIG. 14. (a) The quasiparticle weights Z, (b) kinetic energy E_{kin}, (c) potential energy E_{pot}, and (d) total energy E_{tot} for the degenerate three-orbital model on Bethe lattice for g-RISB with bath size $N_b = 3$, 9, 15 and DMFT-ED with $N_b = 3$, 9 as a function of Coulomb interaction U with Hund's coupling $J = 0.1U$ at filling $n = 2$. The DMFT-CTQMC results at inverse temperature $\beta = 200$ are shown for comparison. The energy unit is the half bandwidth.

and Technology of Taiwan under Grant No. NSTC 112-2112-M-194-007-MY3.

APPENDIX A: ALGORITHM FOR SOLVING G-RISB EQUATIONS

Our algorithm for solving Eqs. (7)–(12) is as follows: (1) starting from an initial guess of R and λ, compute Δ from Eq. (7). (2) Solve D from Eq. (8). (3) Solve λ^c from Eq. (9). (4) Solve $|\Phi\rangle$ from Eq. (10). (5) Compute Δ from Eq. (11). (6) Compute the new R from Eq. (10) and the new λ from Eq. (9). (7) Check the convergence of R and λ. If not converged, go back to step (1). This algorithm is proposed in Ref. [52].

APPENDIX B: CONVERGENCE OF $R^\dagger R$ AND $\Sigma(\infty)$

In this Appendix, we discuss the behavior of the total spectral weight of the correlated degrees of freedom (computed from the variational parameters as $R^\dagger R$) and $\Sigma(\infty)$ as the number of the bath (ghost) orbitals N_b increases.

In Fig. 10, we show the $R^\dagger R$ and $\Sigma(\infty)$ for the degenerate one-orbital $N_{\mathrm{orb}} = 1$, two-orbital $N_{\mathrm{orb}} = 2$, and three-orbital $N_{\mathrm{orb}} = 3$ Hubbard models for the selected Coulomb

interactions and electron fillings. We use the Hubbard-Kanamori type of Coulomb interaction with Hund's coupling fixed at $J = 0.25U$. Our results show that $R^\dagger R$ approaches one and $\Sigma(\infty)$ approaches the Hartree-Fock self-energy, indicated by the horizontal lines, with increasing N_b. Note that $R^\dagger R$ and $\Sigma(\infty)$ are degenerate and diagonal matrices in the considered model.

APPENDIX C: SELF-ENERGY COMPARISON FOR THE DEGENERATE HUBBARD MODELS

The g-RISB self-energy for the one-orbital Hubbard model and the degenerate three-orbital Hubbard model are shown in Figs. 11 and 12, respectively. From our numerical results shown in Figs. 11 and 12, we observed that introducing more ghost (bath) orbitals in g-RISB leads to additional poles in the self-energy, as discussed in the main text. Although the current resolution with $N_b = 15$ is not enough for us to conclude that the g-RISB self-energy converges to the exact DMFT limit, our results in one-orbital Hubbard model $N_{\text{orb}} = 1$ indicates that the poles at higher energy are gradually captured with increasing N_b and the asymptotic behavior of the $\text{Re}\Sigma(\omega)$ at high frequency is improved with increasing N_b. These results suggest that the g-RISB self-energy may capture the incoherent feature with a large enough number of ghost orbitals and a proper broadening factor η. For the degenerate three-orbital Hubbard model $N_{\text{orb}} = 3$, the resolution with $N_b = 15$ is insufficient for comparison with the DMFT-CTQMC self-energy and for drawing conclusions.

The g-RISB self-energy on the Matsubara axis, $z = i\omega_n$, is shown in Fig. 13(a) for the one-band Hubbard model with $U = 2.5$ at half filling $n = 1$, and Fig. 13(b) for the degenerate three-orbital Hubbard model at $U = 1.2$, $J = 0.25U$, and half filling $n = 3$. We consider an infinite-dimensional Bethe lattice. With an increasing number of bath orbitals $N_b = 3$, 5, 15, we observe systematic convergence of the self-energy toward the exact DMFT limit with an increasing number of bath orbitals in both models. Our calculations indicate that the self-energy at $N_b = 15$ is in good quantitative agreement with the DMFT-CTQMC self-energy on the Matsubara axis, both at low and high frequencies.

APPENDIX D: STATIC OBSERVABLES AT $J/U = 0.1$ FOR THE DEGENERATE THREE-ORBITAL HUBBARD MODEL

To demonstrate the accuracy of g-RISB at different regimes of parameters, we show the static observables for the degenerate three-orbital Hubbard model with the ratio $J/U = 0.1$ in Fig. 14. The overall accuracy is similar to the case with ratio $J/U = 0.25$ shown in the main text Fig. 4.

[1] F. Lechermann, A. Georges, G. Kotliar, and O. Parcollet, Phys. Rev. B **76**, 155102 (2007).
[2] A. Isidori and M. Capone, Phys. Rev. B **80**, 115120 (2009).
[3] M. C. Gutzwiller, Phys. Rev. Lett. **10**, 159 (1963).
[4] M. C. Gutzwiller, Phys. Rev. **134**, A923 (1964).
[5] W. Metzner and D. Vollhardt, Phys. Rev. Lett. **62**, 324 (1989).
[6] J. Bünemann, W. Weber, and F. Gebhard, Phys. Rev. B **57**, 6896 (1998).
[7] J. Bünemann and F. Gebhard, Phys. Rev. B **76**, 193104 (2007).
[8] M. Fabrizio, Phys. Rev. B **76**, 165110 (2007).
[9] N. Lanatà, P. Barone, and M. Fabrizio, Phys. Rev. B **78**, 155127 (2008).
[10] G. Kotliar and A. E. Ruckenstein, Phys. Rev. Lett. **57**, 1362 (1986).
[11] T. Li, Y. S. Sun, and P. Wölfle, Z. Phys. B: Condens. Matter **82**, 369 (1991).
[12] L. de' Medici, A. Georges, and S. Biermann, Phys. Rev. B **72**, 205124 (2005).
[13] M. Crispino, M. Chatzieleftheriou, T. Gorni, and L. de' Medici, Phys. Rev. B **107**, 155149 (2023).
[14] R. Yu and Q. Si, Phys. Rev. B **86**, 085104 (2012).
[15] S. Florens and A. Georges, Phys. Rev. B **66**, 165111 (2002).
[16] S. Florens and A. Georges, Phys. Rev. B **70**, 035114 (2004).
[17] A. B. Georgescu and S. Ismail-Beigi, Phys. Rev. B **92**, 235117 (2015).
[18] A. Koga, N. Kawakami, T. M. Rice, and M. Sigrist, Phys. Rev. Lett. **92**, 216402 (2004).
[19] A. Georges, L. de' Medici, and J. Mravlje, Annu. Rev. Condens. Matter Phys. **4**, 137 (2013).
[20] L. de' Medici, J. Mravlje, and A. Georges, Phys. Rev. Lett. **107**, 256401 (2011).
[21] K. Haule and G. Kotliar, New J. Phys. **11**, 025021 (2009).
[22] L. Fanfarillo and E. Bascones, Phys. Rev. B **92**, 075136 (2015).
[23] A. Isidori, M. Berović, L. Fanfarillo, L. de' Medici, M. Fabrizio, and M. Capone, Phys. Rev. Lett. **122**, 186401 (2019).
[24] A. Georges, G. Kotliar, W. Krauth, and M. J. Rozenberg, Rev. Mod. Phys. **68**, 13 (1996).
[25] X. Y. Deng, L. Wang, X. Dai, and Z. Fang, Phys. Rev. B **79**, 075114 (2009).
[26] N. Lanatà, H. U. R. Strand, X. Dai, and B. Hellsing, Phys. Rev. B **85**, 035133 (2012).
[27] N. Lanatà, Y.-X. Yao, C.-Z. Wang, K.-M. Ho, J. Schmalian, K. Haule, and G. Kotliar, Phys. Rev. Lett. **111**, 196801 (2013).
[28] N. Lanatà, Y. Yao, C.-Z. Wang, K.-M. Ho, and G. Kotliar, Phys. Rev. X **5**, 011008 (2015).
[29] N. Lanatà, Y. Yao, X. Deng, V. Dobrosavljević, and G. Kotliar, Phys. Rev. Lett. **118**, 126401 (2017).
[30] N. Lanatà, T.-H. Lee, Y.-X. Yao, V. Stevanović, and V. Dobrosavljević, npj Comput. Mater. **5**, 30 (2019).
[31] C. Piefke and F. Lechermann, Phys. Status Solidi B **248**, 2269 (2011).
[32] C. Piefke and F. Lechermann, Phys. Rev. B **97**, 125154 (2018).
[33] L. de' Medici, G. Giovannetti, and M. Capone, Phys. Rev. Lett. **112**, 177001 (2014).
[34] M. S. Frank, T.-H. Lee, G. Bhattacharyya, P. K. H. Tsang, V. L. Quito, V. Dobrosavljević, O. Christiansen, and N. Lanatà, Phys. Rev. B **104**, L081103 (2021).

[35] J. I. Facio, J. Mravlje, L. Pourovskii, P. S. Cornaglia, and V. Vildosola, Phys. Rev. B **98**, 085121 (2018).

[36] M. E. Barber, F. Lechermann, S. V. Streltsov, S. L. Skornyakov, S. Ghosh, B. J. Ramshaw, N. Kikugawa, D. A. Sokolov, A. P. Mackenzie, C. W. Hicks, and I. I. Mazin, Phys. Rev. B **100**, 245139 (2019).

[37] N. Lanatà, T.-H. Lee, Y.-X. Yao, and V. Dobrosavljević, Phys. Rev. B **96**, 195126 (2017).

[38] N. Lanatà, Phys. Rev. B **105**, 045111 (2022).

[39] E. Fertitta and G. H. Booth, Phys. Rev. B **98**, 235132 (2018).

[40] P. V. Sriluckshmy, M. Nusspickel, E. Fertitta, and G. H. Booth, Phys. Rev. B **103**, 085131 (2021).

[41] Y.-H. Zhang and S. Sachdev, Phys. Rev. Res. **2**, 023172 (2020).

[42] J. R. Moreno, G. Carleo, A. Georges, and J. Stokes, Proc. Natl. Acad. Sci. USA **119**, e2122059119 (2022).

[43] D. Guerci, M. Capone, and M. Fabrizio, Phys. Rev. Mater. **3**, 054605 (2019).

[44] T.-H. Lee, N. Lanatà, and G. Kotliar, Phys. Rev. B **107**, L121104 (2023).

[45] D. Guerci, Ph.D. thesis, International School for Advanced Studies, 2019; https://iris.sissa.it/handle/20.500.11767/103994.

[46] D. Guerci, M. Capone, and N. Lanata, Phys. Rev. Res. **5**, L032023 (2023).

[47] C. Mejuto-Zaera and M. Fabrizio, Phys. Rev. B **107**, 235150 (2023).

[48] S. R. White, Phys. Rev. Lett. **69**, 2863 (1992).

[49] S. R. White, Phys. Rev. B **48**, 10345 (1993).

[50] U. Schollwöck, Rev. Mod. Phys. **77**, 259 (2005).

[51] J. Kanamori, Prog. Theor. Phys. **30**, 275 (1963).

[52] T. Ayral, T.-H. Lee, and G. Kotliar, Phys. Rev. B **96**, 235139 (2017).

[53] N. Lanatà, Phys. Rev. B **108**, 235112 (2023).

[54] Q. Sun, T. C. Berkelbach, N. S. Blunt, G. H. Booth, S. Guo, Z. Li, J. Liu, J. D. McClain, E. R. Sayfutyarova, S. Sharma, S. Wouters, and G. K.-L. Chan, PySCF the Python-based simulations of chemistry framework, WIREs Comput. Mol. Sci. **8**, e1340 (2018).

[55] Q. Sun, X. Zhang, S. Banerjee, P. Bao, M. Barbry, N. S. Blunt, N. A. Bogdanov, G. H. Booth, J. Chen, Z.-H. Cui, J. J. Eriksen, Y. Gao, S. Guo, J. Hermann, M. R. Hermes, K. Koh, P. Koval, S. Lehtola, Z. Li, J. Liu *et al.*, Recent developments in the PySCF program package, J. Chem. Phys. **153**, 024109 (2020).

[56] H. Zhai and G. K.-L. Chan, J. Chem. Phys. **154**, 224116 (2021).

[57] H. Zhai, H. R. Larsson, S. Lee, Z.-H. Cui, T. Zhu, C. Sung, L. Peng, R. Peng, K. Liao, J. Tölle, J. Yang, S. Li, and G. K.-L. Chan, J. Chem. Phys. **159**, 234801 (2023).

[58] S. Y. Savrasov, K. Haule, and G. Kotliar, Phys. Rev. Lett. **96**, 036404 (2006).

[59] M. Caffarel and W. Krauth, Phys. Rev. Lett. **72**, 1545 (1994).

[60] M. J. Rozenberg, G. Moeller, and G. Kotliar, Mod. Phys. Lett. B **08**, 535 (1994).

[61] A. Liebsch, Phys. Rev. Lett. **95**, 116402 (2005).

[62] C. A. Perroni, H. Ishida, and A. Liebsch, Phys. Rev. B **75**, 045125 (2007).

[63] H. Ishida and A. Liebsch, Phys. Rev. B **81**, 054513 (2010).

[64] A. Liebsch and H. Ishida, J. Phys.: Condens. Matter **24**, 053201 (2012).

[65] M. Capone, M. Civelli, S. S. Kancharla, C. Castellani, and G. Kotliar, Phys. Rev. B **69**, 195105 (2004).

[66] M. Civelli, M. Capone, S. S. Kancharla, O. Parcollet, and G. Kotliar, Phys. Rev. Lett. **95**, 106402 (2005).

[67] B. Kyung, S. S. Kancharla, D. Sénéchal, A.-M. S. Tremblay, M. Civelli, and G. Kotliar, Phys. Rev. B **73**, 165114 (2006).

[68] A. Amaricci, L. Crippa, A. Scazzola, F. Petocchi, G. Mazza, L. de' Medici, and M. Capone, Comput. Phys. Commun. **273**, 108261 (2022).

[69] S. Iskakov and M. Danilov, Comput. Phys. Commun. **225**, 128 (2018).

[70] M. Capone, L. de' Medici, and A. Georges, Phys. Rev. B **76**, 245116 (2007).

[71] O. Parcollet, M. Ferrero, T. Ayral, H. Hafermann, I. Krivenko, L. Messio, and P. Seth, Comput. Phys. Commun. **196**, 398 (2015).

[72] P. Seth, I. Krivenko, M. Ferrero, and O. Parcollet, Comput. Phys. Commun. **200**, 274 (2016).

[73] E. Gull, A. J. Millis, A. I. Lichtenstein, A. N. Rubtsov, M. Troyer, and P. Werner, Rev. Mod. Phys. **83**, 349 (2011).

[74] C. Melnick, P. Sémon, K. Yu, N. D'Imperio, A.-M. Tremblay, and G. Kotliar, Comput. Phys. Commun. **267**, 108075 (2021).

[75] M. Chatzieleftheriou, A. Kowalski, M. Berović, A. Amaricci, M. Capone, L. De Leo, G. Sangiovanni, and L. de' Medici, Phys. Rev. Lett. **130**, 066401 (2023).

[76] A. Tamai, M. Zingl, E. Rozbicki, E. Cappelli, S. Riccò, A. de la Torre, S. McKeown Walker, F. Y. Bruno, P. D. C. King, W. Meevasana, M. Shi, M. Radović, N. C. Plumb, A. S. Gibbs, A. P. Mackenzie, C. Berthod, H. U. R. Strand, M. Kim, A. Georges, and F. Baumberger, Phys. Rev. X **9**, 021048 (2019).

[77] X. Deng, K. Haule, and G. Kotliar, Phys. Rev. Lett. **116**, 256401 (2016).

[78] C. Bergemann, A. P. Mackenzie, S. R. Julian, D. Forsythe, and E. Ohmichi, Adv. Phys. **52**, 639 (2003).

[79] P. Hohenberg and W. Kohn, Phys. Rev. **136**, B864 (1964).

[80] W. Kohn and L. J. Sham, Phys. Rev. **140**, A1133 (1965).

[81] N. Marzari, A. A. Mostofi, J. R. Yates, I. Souza, and D. Vanderbilt, Rev. Mod. Phys. **84**, 1419 (2012).

[82] P. Blaha, K. Schwarz, F. Tran, R. Laskowski, G. K. H. Madsen, and L. D. Marks, J. Chem. Phys. **152**, 074101 (2020).

[83] T. Vogt and D. J. Buttrey, Phys. Rev. B **52**, R9843(R) (1995).

[84] P. E. Blöchl, O. Jepsen, and O. K. Andersen, Phys. Rev. B **49**, 16223 (1994).

[85] J. Kuneš, R. Arita, P. Wissgott, A. Toschi, H. Ikeda, and K. Held, Comput. Phys. Commun. **181**, 1888 (2010).

[86] G. Pizzi, V. Vitale, R. Arita, S. Blügel, F. Freimuth, G. Géranton, M. Gibertini, D. Gresch, C. Johnson, T. Koretsune, J. Ibañez-Azpiroz, H. Lee, J.-M. Lihm, D. Marchand, A. Marrazzo, Y. Mokrousov, J. I Mustafa, Y. Nohara, Y. Nomura, L. Paulatto *et al.*, J. Phys.: Condens. Matter **32**, 165902 (2020).

[87] J. Mravlje, M. Aichhorn, T. Miyake, K. Haule, G. Kotliar, and A. Georges, Phys. Rev. Lett. **106**, 096401 (2011).

[88] M. Kim, J. Mravlje, M. Ferrero, O. Parcollet, and A. Georges, Phys. Rev. Lett. **120**, 126401 (2018).

[89] H. J. Lee, C. H. Kim, and A. Go, Phys. Rev. B **102**, 195115 (2020).

[90] F. B. Kugler, M. Zingl, H. U. R. Strand, S.-S. B. Lee, J. von Delft, and A. Georges, Phys. Rev. Lett. **124**, 016401 (2020).

[91] X. Cao, Y. Lu, P. Hansmann, and M. W. Haverkort, Phys. Rev. B **104**, 115119 (2021).

[92] G. Kotliar, S. Y. Savrasov, K. Haule, V. S. Oudovenko, O. Parcollet, and C. A. Marianetti, Rev. Mod. Phys. **78**, 865 (2006).
[93] S. Y. Savrasov and G. Kotliar, Phys. Rev. B **69**, 245101 (2004).
[94] T. L. Gilbert, Phys. Rev. B **12**, 2111 (1975).
[95] R. Chitra and G. Kotliar, Phys. Rev. B **62**, 12715 (2000).
[96] R. Adler, C. Melnick, and G. Kotliar, Comput. Phys. Commun. **294**, 108907 (2024).
[97] T.-H. Lee, N. Lanatà, M. Kim, and G. Kotliar, Phys. Rev. X **11**, 041040 (2021).
[98] D. Bauernfeind, M. Zingl, R. Triebl, M. Aichhorn, and H. G. Evertz, Phys. Rev. X **7**, 031013 (2017).